



# Effect of various strategies of soc-dependent operating current on performance of a vanadium redox flow battery



W.W. Yang<sup>\*</sup>, F.Y. Yan, Z.G. Qu, Y.L. He

Key Laboratory of Thermo-Fluid Science and Engineering of Ministry of Education, School of Energy and Power Engineering, Xi'an Jiaotong University, PR China

## ARTICLE INFO

### Article history:

Received 23 June 2017

Received in revised form

31 August 2017

Accepted 31 October 2017

Available online 4 November 2017

### Keywords:

Vanadium redox flow battery

Soc-dependent operating current

Overall performance

Mathematical modeling

## ABSTRACT

A two-dimensional quasi-steady-state model is applied to investigate charge/discharge behavior and performance of a VRFB. Emphasis is focused on exploring the influences of various strategies of soc-dependent operating current density on battery performance. For constant-current operation, with the increase of current density, although the system mean power density is significantly boosted, the system capacity and net discharge energy in a cycle are obviously decreased. It is quite difficult to give consideration to both the system capacity and system power simultaneously such that overall battery performance can be improved. Applying the strategy of soc-dependent operating current (i.e., low current at the end of charge/discharge process while high current for the rest time), the system capacity, power density and net discharge energy in a cycle can be simultaneously boosted while comparable efficiencies can be achieved. Optimally, at the mean operating current density of about  $70 \text{ mA cm}^{-2}$ , the system capacity is maximally improved by 9.3% and the net discharge energy is maximally increased by 7.9% as compared with that under constant-current operation. As the same time, the energy-based system efficiency can be maintained over 78%, which is comparable with that for constant-current operation.

© 2017 Elsevier Ltd. All rights reserved.

## 1. Introduction

Redox flow battery (RFB) has been regarded as a promising electricity storage technology for the stabilization of grid electricity supplies, emergency power backup, and intermittent power system [1–4], due to its virtues of long cycle-life and flexibilities of energy and power ratings. Although great progress has been made in advancing the RFB technology especially the all-vanadium redox flow battery (VRFB) technology, the problems associated with improving the battery performance in term of system capacity, power and efficiency, and the difficulties in optimizing the battery structures and operating parameters are still remained and needs to be resolved.

During the past decade, extensive efforts have been paid to develop the advanced component materials with excellent properties for the electrode, electrolyte and membrane of a VRFB [5–7]. Besides, the improvement of battery performance also relies on addressing critical transport issues and optimizing cell structure. To

achieve this, many investigations [8–20] have also been conducted on understanding the characteristics of physical properties distribution inside the VRFB, revealing critical transport processes, and examining the impacts of different cell structure designs on battery performance.

In addition, there are also some studies on optimizing the operating parameters of battery in order to boost the battery charge/discharge performance [21–25]. As we know, during battery operation, the species concentration in the electrolyte tank (corresponding to inlet condition for both electrodes) changes with time in a charge-discharge cycle. The concentrations of active reactant species decrease as the charge/discharge process undergoes, which are even approaching zero at the end of charge or discharge process. It is thus critical to increase the mass transport at the end of charge or discharge process. Ma et al. [24] fabricated a kilo-watt-class VRFB to investigate various strategies of electrolyte flow rate on battery charge/discharge behavior and performance. They proposed flow rate step-up strategy for operating VRFB system which maintains a constant flow rate throughout main operating state-of-charge while stepping up the flow rate at the end of charge or discharge process. By doing this, the battery performance

<sup>\*</sup> Corresponding author.

E-mail address: [yangww@mail.xjtu.edu.cn](mailto:yangww@mail.xjtu.edu.cn) (W.W. Yang).

can be improved. In addition, a zero-dimensional model was presented by Tang et al. [25] to demonstrate the feasibility of fully variable flow rate throughout a charge-discharge cycle. The results indicated that variable flow rates are superior to constant flow rates for given system design.

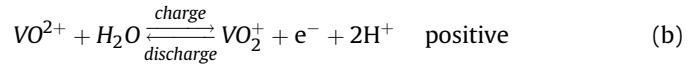
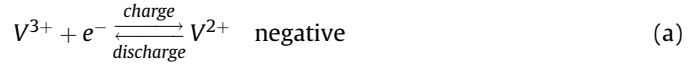
The operating current density is also an important parameter that influences the charge/discharge behavior and performance of a VRFB. Lowering the operating current may extend the charge/discharge depth and improve theoretical round-trip efficiency of battery because of the decreased voltage losses. However, the charge/discharge time is usually very long for low-current operation, which in turn increases the pump work consumption. On the contrary, increasing the operating current density, the system power can be increased but the voltage losses are also increased, showing adverse impact on system efficiency. Some studies [26–29] revealed that both the positive and negative electrode overpotentials vary with time (i.e. corresponding to various state of charge) in a charge-discharge cycle and they were increased at the beginning and the end of charge/discharge process. It is thus essential to optimize the strategy of variable operating current such that battery performance in terms of capacity, power density, efficiency, and net discharge energy in a cycle can be simultaneously boosted. Currently, the related study is scarce.

In present study, a two-dimensional (2-D) quasi-steady-state mathematical model is presented for simulating coupled mass-species-charge transfer and electrochemical reactions in a VRFB. The charge/discharge behaviors and performance of a VRFB under constant-current operation were firstly analyzed. Emphasis is located on examining the influences of various strategies of variable (i.e., soc-dependent) operating current density on overall charge/discharge performance of a VRFB.

## 2. Mathematical model

Consider a 2-D domain as indicated in Fig. 1, which represents the core of VRFB consisting of negative carbon plate, negative electrode, membrane, positive electrode and positive carbon plate. An electrolyte consisting of vanadium ions dissolved in a sulfuric acid solution are stored in respective electrolyte tank and circulated to the battery. In Fig. 1, x-axis represents the direction across the

membrane, while y-axis is the electrolyte flow direction in the flow-through carbon-felt electrode. During the charge/discharge of VRFB, reactants are depleted while products are generated due to electrode reactions, causing the concentration variation of vanadium ions along flow direction. The reaction in each flow-through carbon felt electrode can be expressed as:



The 2-D consideration can save the computational time without losing much accuracy. To simplify the model, following assumptions are involved including:

- (1) Vanadium ions crossover through the membrane and the resultant side reactions are neglected;
- (2) Possible side reactions such as hydrogen and oxygen evolutions and the accompanying gas bubble formation in the electrodes are not considered;
- (3) In each charge-discharge cycle, the VRFB is charged and discharged to cutoff voltages of 1.7 V and 1.1 V;
- (4) The dilute-solution approximation is applied to model the species transport in electrolyte solution.

### 2.1. Model formulation

#### 2.1.1. Transport in the porous electrode

The molar flux of species  $i$  including  $VO_2^+$ ,  $VO^{2+}$ ,  $V^{3+}$ ,  $V^{2+}$  (marked with  $V_5$ ,  $V_4$ ,  $V_3$ ,  $V_2$ , respectively) and  $H^+$  in the porous electrode can be described by a modified Nernst-Planck equation, which is given by

$$N_i = -D_i^{eff} \nabla C_i - \frac{z_i F C_i D_i}{RT} \nabla \phi_e + \vec{u} C_i \quad (1)$$

where  $\phi_e$  is the ionic potential in electrolyte phase,  $D_i^{eff}$  is the effective diffusion coefficient of species  $i$  given by  $D_i^{eff} = \varepsilon^{3/2} D_i^0$ ,  $z_i$  is the valence for species  $i$ ,  $C_i$  is the concentration of species  $i$  in bulk electrolyte solution,  $\vec{u}$  is the superficial velocity vector in the porous electrode, which is related to pressure gradient according to Darcy's law for porous medium flow.

Mathematically, the conservation of species  $i$  can thus be formulated as

**Table 1**

Sources terms for mass, momentum, species and charge conservation equations.

Source terms	Negative electrode		Positive electrode	
	Variable	Expression	Variable	Expression
$R_i$	$V^{2+}$	$-\frac{j_{neg}}{F}$	$VO_2^+$	$-\frac{j_{pos}}{F}$
	$V^{3+}$	$\frac{j_{neg}}{F}$	$VO^{2+}$	$\frac{j_{pos}}{F}$
	$H^+$	$-\frac{j_{cell}}{\delta_{neg}}$	$H^+$	$\frac{j_{cell}}{\delta_{pos}} - \frac{2j_{pos}}{F}$
$S_\phi$	$\phi_e$	$j_{neg}$	$\phi_e$	$-j_{pos}$
	$\phi_s$	$j_{neg}$	$\phi_s$	$-j_{pos}$
$\dot{m}$	-	$\frac{M_w N_{w,cross}}{\delta_{neg}}$	-	$\frac{M_w N_{w,cross}}{\delta_{pos}}$

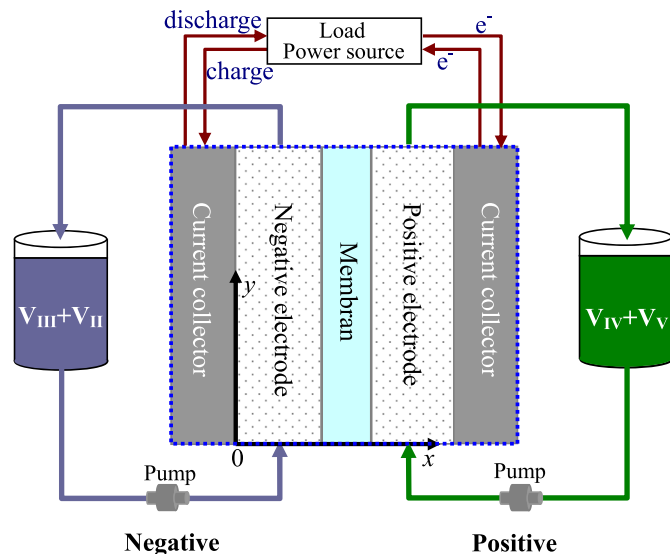


**Fig. 1.** Schematic of all-vanadium redox flow battery and computational domain of present model.

$$\frac{\varepsilon \partial C_i}{\partial t} + \nabla \cdot (\vec{u} C_i) = \nabla \cdot (D_i^{eff} \nabla C_i) + \nabla \cdot \left( \frac{z_i F C_i D_i}{RT} \nabla \phi_e \right) + R_i \quad (2)$$

where  $R_i$  is general source term, representing the generation rate of species  $i$  as listed in Table 1. In Eq. (2), the transient term (i.e., the first term on the left-hand side of equation) is actually approximate to be the time-dependent concentration variation of species  $i$  at the inlet [28]. Mathematically, it can be estimated by

$$\frac{\varepsilon \partial C_i}{\partial t} \approx \frac{\varepsilon I_{cell} A_{cell}}{V_{tank} F} \quad (3)$$

where  $A_{cell}$  is the battery area,  $V_{tank}$  is the volume of electrolyte solution for each electrode, and  $I_{cell}$  is the operating current density, which is set to be negative for charge process but positive for discharge process when considering the change in the current direction.

With respect to the concentration of  $SO_4^{2-}$  ion, it can be simply estimated by considering electrically neutral condition of the electrolyte solution.

The flow of electrolyte solution through the porous electrodes is simulated by considering the overall mass conservation law and Darcy's law for flow in porous medium, i.e.,

$$-\nabla \cdot \left( \frac{\rho}{\mu} \cdot \frac{d_f^2 \varepsilon^3}{k_{CK} (1 - \varepsilon)^2} \nabla p \right) = \dot{m} \quad (4)$$

where  $\dot{m}$  is the equivalent mass generation rate,  $p$  is the pressure of electrolyte solution,  $d_f$  is the fiber diameter and  $k_{CK}$  is the Carman-Kozeny constant related to the type of porous medium [27].

The transfer of charged ions in the electrolyte solution results in the ionic current. Since the thin-layer feature of the electrode membrane assembly of the VRFB with flow-through carbon-felt electrode, local ionic current mainly transfers through the thickness of electrode along  $x$  direction. As a result, the ionic potential in the electrolyte phase mainly varies along  $x$ -direction. Herein, let  $\vec{T}_e$  be local ionic current density, the conservation of the ionic current can be expressed as

$$\frac{d}{dx} \vec{T}_e = -\sigma_e^{eff} \frac{d^2 \phi_e}{dx^2} = \frac{\int_0^L S_\phi dy}{L} \quad (5)$$

where  $S_\phi$  is the source term for charge generation as defined in Table 1,  $\phi_e$  is ionic potential in electrolyte phase, and  $\sigma_e^{eff}$  is effective ionic conductivity of electrolyte phase, which can be calculated by

$$\sigma_e^{eff} = \frac{F^2}{RT} \sum_i z_i^2 D_i^{eff} C_i \quad (6)$$

Local ionic current density and ionic potential in the electrolyte phase can be analyzed by integrating Eq. (5) along  $x$ -direction. And the ohmic loss due to the ionic current through electrode along  $x$ -direction,  $\eta_{ohm,e}$ , can then be estimated.

The charge entering (or leaving) the electrolyte phase is balanced by the charge leaving (or entering) the solid electron-conducting phase. It is assumed that the electronic current also mainly flows through the porous electrode along  $x$ -direction. Let  $\vec{T}_s$  be the local electronic current density, we then have,

$$\frac{d}{dx} \vec{T}_s = -\sigma_s^{eff} \frac{d^2 \phi_s}{dx^2} = \frac{\int_0^L S_\phi dy}{L} \quad (7)$$

where  $\sigma_s^{eff}$  denotes the effective electronic conductivity of porous electrode calculated by the Bruggemann correction, i.e.,  $\sigma_s^{eff} = \sigma_s (1 - \varepsilon)^{1.5}$ .

Integrating Eq. (7), the electronic potential drop across the electrode, representing the ohmic voltage loss due to electron transport,  $\eta_{ohm,s}$ , can be calculated.

### 2.2.1. Transport through the membrane

The transfer of proton through the membrane results in the ionic current. According to ohmic law, we have

$$\vec{T}_m = -\sigma_m \frac{d\phi_m}{dx} \quad (8)$$

where  $\sigma_m$  and  $\phi_m$  are, respectively, the proton conductivity and ionic potential in the membrane.

Consequently, the voltage loss due to proton transport across the membrane,  $\eta_{ohm,m}$ , can be simply calculated by

$$\eta_{ohm,m} = I_{cell} \frac{\delta_m}{\sigma_m} \quad (9)$$

The transfer of water through the membrane is considered by electro-osmotic drag mode because water pressure difference and concentration difference across the membrane are both negligible, which gives

$$N_{w,cross} = n_{d,w} \frac{I_{cell}}{F} \quad (10)$$

where  $n_{d,w}$  is the drag coefficient of water per proton. The amount of water crossover is finally used in calculating the general source term of Eq. (4). In a charge-discharge cycle, liquid water is transferred from positive electrode to negative electrode during charge process, whereas it is reversed during the discharge process. The problem of water crossover leads to the imbalance of electrolyte solutions.

### 2.1.3. Model for the electrolyte solution in the tank

Total amount of vanadium ions in each electrolyte tank keeps unchanged during battery operation when vanadium ions crossover is not considered, the presence of water crossover causes volume imbalance of negative and positive solutions. The total vanadium ions concentration needs to be corrected with considering the dilution or concentration effect. The concentration correction factors (i.e., dilution or concentrating factors) for negative and positive electrolyte solution in the tank during charge/discharge process are, respectively, estimated by

$$\xi_{neg} = \frac{V_{tank,neg}^0}{V_{tank,neg}^0 - \int_{t=0}^t \frac{M_w A_{cell} N_{w,cross}}{\rho_w} dt} \quad (11)$$

and

$$\xi_{pos} = \frac{V_{tank,pos}^0}{V_{tank,pos}^0 + \int_{t=0}^t \frac{M_w A_{cell} N_{w,cross}}{\rho_w} dt} \quad (12)$$

where  $V_{tank,neg}^0$  and  $V_{tank,pos}^0$  are, respectively, the electrolyte volume

in positive and negative electrolyte tank.

## 2.2. Boundary conditions

The parameter of *soc* is used to indicate the state of charge for the battery, which is defined by

$$soc = \frac{C_{V_2}}{C_{V,neg}} = \frac{C_{V_5}}{C_{V,pos}} \quad (13)$$

where  $C_{V,neg}$  and  $C_{V,pos}$  are, respectively, the total vanadium ion concentrations in negative and positive electrolyte tank.

Mathematically, the change in *soc* during charge/discharge process is proportionally related to charge/discharge time, applied current as well as the total vanadium ion concentrations, which is given by

$$dsoc = -\frac{I_{cell}A_{cell}}{FV_{tank}^0C_V^0}dt \quad (14)$$

where  $C_V^0$  is initial total vanadium ion concentration in either negative or positive electrolyte tank, and  $V_{tank}^0$  is the total electro-

---


$$j_{pos} = A_{s,pos}Fk_{pos}(C_{V_4}C_{V_5})^{0.5} \left[ \frac{C_{V_5}^s}{C_{V_5}} \exp\left(\frac{0.5F\eta_{pos}}{RT}\right) - \frac{C_{V_4}^s}{C_{V_4}} \exp\left(-\frac{0.5F\eta_{pos}}{RT}\right) \right] \quad (22)$$


---

and

---


$$j_{neg} = A_{s,neg}Fk_{neg}(C_{V_2}C_{V_3})^{0.5} \left[ \frac{C_{V_2}^s}{C_{V_2}} \exp\left(\frac{0.5F\eta_{neg}}{RT}\right) - \frac{C_{V_3}^s}{C_{V_3}} \exp\left(-\frac{0.5F\eta_{neg}}{RT}\right) \right] \quad (23)$$


---

lyte volume in either negative or positive electrolyte tank. Initially, *soc* is set to be 0.03 at the beginning for starting the charge-discharge cycle. Generally, three charge-discharge cycles are simulated with a *soc* step of 0.005. For each cycle, the cut-off voltages for ending the charge or discharge process are, respectively, set to be 1.7 V and 1.1 V.

For quasi-steady-state simulation, the inlet concentration of each species for both electrodes (i.e.,  $y = 0$ ) is given based on supplying conditions at any *soc*, i.e.,

$$C_{V_4}^n = [C_{V,pos}^0(1 - soc)]\xi_{pos} \quad (15)$$

$$C_{V_5}^n = [C_{V,pos}^0soc]\xi_{pos} \quad (16)$$

$$C_{V_2}^n = [C_{V,neg}^0soc]\xi_{neg} \quad (17)$$

$$C_{V_3}^n = [C_{V,neg}^0(1 - soc)]\xi_{neg} \quad (18)$$

$$C_{H^+,neg}^n = [C_{H^+,neg}^0 + C_{V,neg}^0(soc^0 - soc)]\xi_{neg} \quad (19)$$

$$C_{H^+,pos}^n = [C_{H^+,pos}^0 + C_{pos,V}^0(soc^0 - soc)]\xi_{pos} \quad (20)$$

where  $soc^0$  is the initial state of charge for charge process or discharge process.

The superficial velocities at inlets of both electrodes are, respectively, given by

$$v_{in} = \frac{Q}{A_{cross}} \quad (21)$$

where  $Q$  is electrolyte flow rate and  $A_{cross}$  is cross-section area of electrode.

At the outlets of both electrodes (i.e.,  $y = L$ ), the gradients of species concentration as well as the fluid velocity along  $y$ -direction are all set to be zero.

At interfaces between porous electrode and carbon plate, the impermeable-wall condition for species, mass transfer and non-slip condition for fluid flow are specified. The internal interfacial conditions between different layers in VFRB are given based on the principle of continuity and mass-species flux balance.

## 2.3. Electrochemical kinetics

The transfer current densities for positive and negative electrode reactions are formulated by using the Butler-Volmer expressions, which are

where  $A_s$  is the specific reaction areas of electrode,  $C_i^s$  is the concentration of species  $i$  at active surface,  $\eta$  is the overpotential due to electrode reaction.

With invoking local mass transfer coefficient, the transfer of species between bulk solution in the pores and active surface (i.e., liquid-solid interface) can also be modeled [28], and the transfer rate of species from bulk solution to active surface is physically balanced by mass consumption rate of species by electrode reactions. Finally, the species concentration at active surface is expressed as a function of species concentration in bulk solution as shown in Table 2.

## 2.4. Current balance and battery voltage

During the charge or discharge process, the electrons transfer from/to negative electrode through the external circuit to/from positive electrode. The balance of battery current density between negative and positive electrodes can be given by

$$I_{cell} = \frac{\iint_{neg} j_{neg} dx dy}{L} = \frac{\iint_{pos} j_{pos} dx dy}{L} \quad (24)$$

For a given applied current density, overpotentials due to electrode reactions can be determined with the help of Eqs. (22)–(24). As for ohmic loss, it includes the ohmic voltage loss due to ionic current transport through the electrolyte and the membrane, and ohmic voltage loss due to electronic current transport through porous electrode. Finally, the battery charge/discharge voltage at a

**Table 2**

Expressions for species concentration at active reaction surface.

Species concentration at active reaction surface	Expressions for the constants
$\frac{C_{V_4}}{C_{V_4}} = \frac{A_1 C_{V_4} / C_{V_4} + (1 + A_1)}{1 + A_1 + B_1}$	$A_1 = \frac{k_{pos}}{k_m} \left( \frac{C_{V_4}}{C_{V_5}} \right)^{0.5} \exp\left(\frac{0.5F\eta_{pos}}{RT}\right)$
$\frac{C_{V_5}}{C_{V_5}} = \frac{B_1 C_{V_4} / C_{V_5} + (1 + B_1)}{1 + A_1 + B_1}$	$B_1 = \frac{k_{pos}}{k_m} \left( \frac{C_{V_5}}{C_{V_4}} \right)^{0.5} \exp\left(-\frac{0.5F\eta_{pos}}{RT}\right)$
$\frac{C_{V_3}}{C_{V_3}} = \frac{A_2 C_{V_3} / C_{V_3} + (1 + A_2)}{1 + A_2 + B_2}$	$A_2 = \frac{k_{neg}}{k_m} \left( \frac{C_{V_3}}{C_{V_2}} \right)^{0.5} \exp\left(\frac{0.5F\eta_{neg}}{RT}\right)$
$\frac{C_{V_2}}{C_{V_2}} = \frac{B_2 C_{V_3} / C_{V_2} + (1 + B_2)}{1 + A_2 + B_2}$	$B_2 = \frac{k_{neg}}{k_m} \left( \frac{C_{V_2}}{C_{V_3}} \right)^{0.5} \exp\left(-\frac{0.5F\eta_{neg}}{RT}\right)$

certain applied current density can be determined by

$$E_{cell} = E_{eq} - \eta_{neg} - \eta_{pos} - (\eta_{ohm,e} + \eta_{ohm,s} + \eta_{ohm,m}) \quad (25)$$

where  $E_{eq}$  is the equilibrium open circuit voltage of a VRFB, which is calculated by a complete form of Nernst equation [30].

$$E_{eq} = E_0 + \frac{RT}{F} \ln \left( \frac{C_{V_5} \cdot C_{V_2} \cdot (C_{H^+,pos})^2}{C_{V_4} \cdot C_{V_3} \cdot C_{H^+,neg}} \right) \quad (26)$$

with  $E_0$  being the standard thermodynamic theoretical voltage of a VRFB.

## 2.5. Performance parameters

To evaluate the performance of a VRFB, the parameters including system capacity, power density, charge/discharge energy in a cycle and system efficiency are analyzed.

As mentioned earlier, the applied current density of battery,  $I_{cell}$ , is set to be negative for charge process and positive for discharge process due to the switch of current direction. If only considering the magnitude of operational current density, absolute value of applied current density is involved the following.

The system charge capacity, which is theoretically equal to discharge capacity without considering self discharge, can be calculated by

$$Cap. = \int_{t_{char, start}}^{t_{char, end}} I_{cell} A_{cell} dt \quad (27)$$

For variable operating current density, the mean operating current density for either charge or discharge process, is defined as

$$\bar{I}_{cell} = \frac{\int_{t_{start}}^{t_{end}} I_{cell} dt}{\int_{t_{start}}^{t_{end}} dt} \quad (28)$$

As for system power density, the mean charge or discharge power density is calculated by

$$\bar{P} = \frac{\int_{t_{start}}^{t_{end}} I_{cell} E_{cell} dt}{\int_{t_{start}}^{t_{end}} dt} \quad (29)$$

For a charge-discharge cycle, theoretically, the round-trip efficiency of the battery can be given by

$$RE = \frac{\int_{t_{dis, start}}^{t_{dis, end}} I_{cell} A_{cell} E_{cell, dis} dt}{\int_{t_{char, start}}^{t_{char, end}} I_{cell} A_{cell} E_{cell, char} dt} \quad (30)$$

Taking into account the pump work consumption, energy-based system efficiency can be defined as

$$SE = \frac{W_{dis}}{W_{char}} = \frac{\int_{t_{dis, start}}^{t_{dis, end}} I_{cell} A_{cell} E_{cell, dis} dt - \int_{t_{dis, start}}^{t_{dis, end}} (P_{pump, neg} + P_{pump, pos}) dt}{\int_{t_{char, start}}^{t_{char, end}} I_{cell} A_{cell} E_{cell, char} dt + \int_{t_{char, start}}^{t_{char, end}} (P_{pump, neg} + P_{pump, pos}) dt} \quad (31)$$

where  $W_{dis}$  is the net output work for discharge process and  $W_{char}$  is the total work for charge process. The pump work consumption can be estimated by

$$P_{pump} = Q \Delta p / \zeta_{pump} \quad (32)$$

with  $\zeta_{pump}$  being pump efficiency, which is assumed to be 0.9.

## 2.6. Numerical details and parameters

The concerned information of the mass/species transport in a VRFB during a charge/discharge cycle can be obtained by numerically solving the above governing equations with specific boundary conditions, basic geometrical and operating parameters in Table 3 and physicochemical properties (listed in Table 4).

To solve above governing equations, a self-written code based on the SIMPLE algorithm with the Finite-Volume-Method, all the variables are iteratively solved until the pre-set convergent criterions are reached. In the program, the relative error tolerance is set to be  $1 \times 10^{-6}$ .

## 3. Results and discussion

### 3.1. Model validation

The simulated battery voltages are compared against experimental data in order to validate the model. Fig. 2 shows the variation of charge/discharge voltage of battery for a charge-discharge cycle with soc at the current densities of 40 and 80 mA cm<sup>-2</sup>. Generally, the simulations can well capture the variation trends of battery voltage with soc. Within the soc range from 0.05 to 0.95, the simulated battery voltages are in good agreement with experimental data found in Ref. [27]. It is noticed that the present model eliminates the treatment [27] where a value of 140 mV is added to



**Table 3**  
Geometric dimensions and operating parameters.

Parameters	Symbols	Value	Unit
Thickness of electrode	$\delta$	$3 \times 10^{-3}$	m
Length of electrode	$L$	$3 \times 10^{-2}$	m
Width of electrode	$W$	$2.5 \times 10^{-2}$	m
Thickness of membrane	$\delta_{mem}$	125	um
Electrode porosity	$\epsilon$	0.68	-
Operating temperature	$T$	298	K
Electrolyte volume of each electrode	$V$	30	ml
Volumetric flow rate of electrolyte in each electrode	$Q$	1.0	ml s <sup>-1</sup>
Operating current density	$I_{cell}$	20–80	mA cm <sup>-2</sup>
Initial total vanadium concentration in negative electrode	$C_{V,neg}^0$	1500	mol m <sup>-3</sup>
Initial total vanadium concentration in positive electrode	$C_{V,pos}^0$	1500	mol m <sup>-3</sup>
Initial proton concentration in negative electrode	$C_{H^+,neg}^0$	4500	mol m <sup>-3</sup>
Initial proton concentration in positive electrode	$C_{H^+,pos}^0$	6000	mol m <sup>-3</sup>
Operating temperature	$T$	298	K

the simulated voltage in order to match experiment result. The remained discrepancy between the present numerical results and experimental data may be attributed to the ignorance of side reactions, other model simplification and uncertainties of model parameters.

### 3.2. Charge/discharge behavior under constant-current operation

The charge/discharge behaviors of a VRFB for various current densities (i.e., 20, 40, 60 and 80 mA cm<sup>-2</sup>) are explored in this section. In the simulations, three charge-discharge cycles are conducted. In each charge-discharge cycle, the VRFB was charged to the upper voltage limit of 1.7 V which is then switched to discharge process until the pre-set cut-off limit of 1.1 V was reached. In this study, the voltage evolution profile of the second cycle is analyzed.

Fig. 3a displays the charge/discharge voltage profiles for various current densities of 20, 40, 60 and 80 mA cm<sup>-2</sup>. As shown in Fig. 3a, the total charge/discharge time is dramatically decreased with the increase of current density. It is seen that increasing current density, the whole voltage curve is elevated for charge process and lowered for discharge process mainly due to the increased

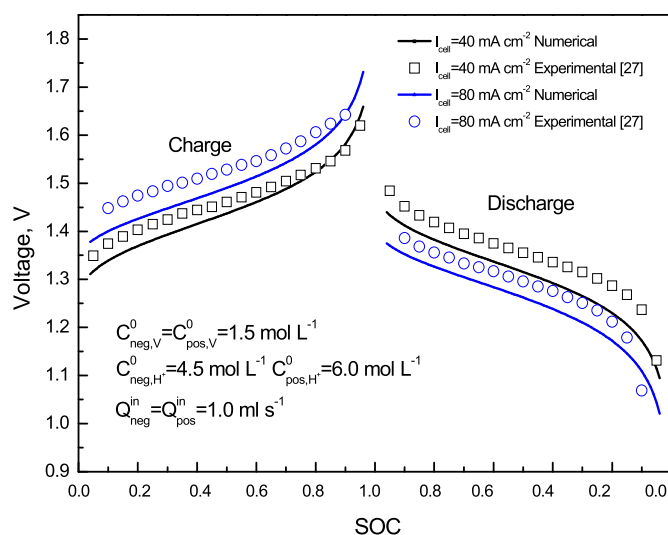


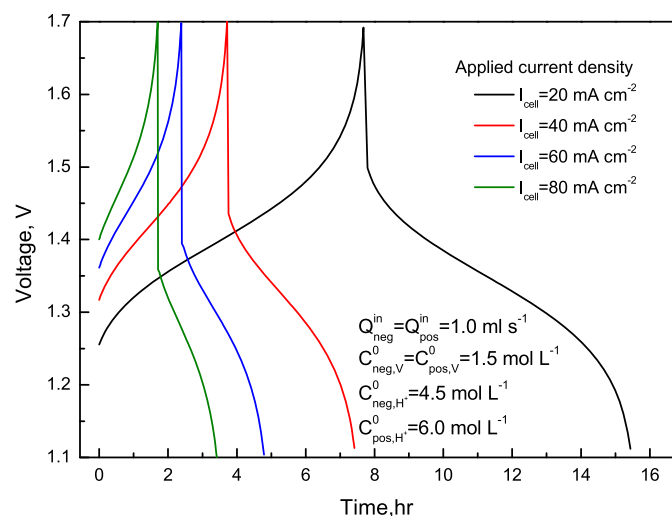
**Fig. 2.** Comparison between simulated and measured charge/discharge curves at current densities of 40 and 80 mA cm<sup>-2</sup>.

activation and ohmic polarizations. Also, the electrolyte transfer is insufficient at the end of charge/discharge process because of the depletion of active reactants, resulting in severe concentration polarization especially at higher current density. This in turn drives up the battery voltage to its cut-off limit faster and attenuates the deepness for charge process and discharge process. This consequence can be illustrated by plotting the corresponding evolution curve of soc in a charge-discharge cycle as shown in Fig. 3b. Clearly, as can be seen, the charge/discharge depths are obviously debated with the increase of current density. For example, the ending soc can be deepened to 0.03 for discharge process when cut-off potential is triggered at the current density of 20 mA cm<sup>-2</sup>, whereas the ending soc is 0.105 for discharge process at the current density of 80 mA cm<sup>-2</sup>. As the result of the reduced operational window of soc for high current density, the corresponding charge/discharge capacity will be definitely reduced.

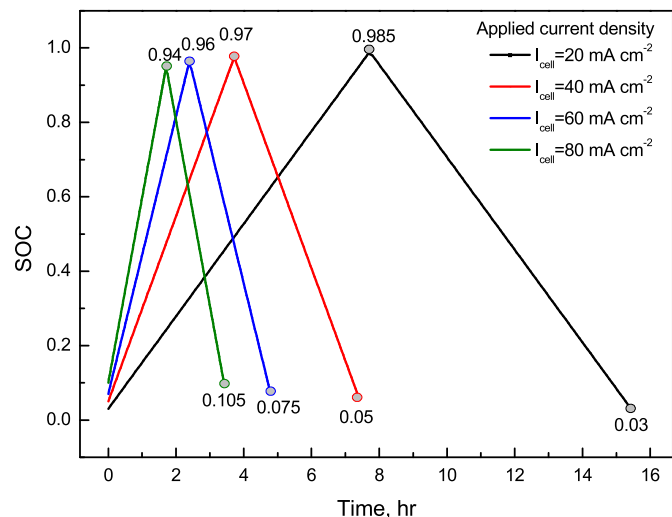
Variations of total electrode overpotential with soc in a charge-discharge cycle at various current densities of 20, 40, 60 and 80 mA cm<sup>-2</sup> are also illustrated in Fig. 4. As can be seen, clearly, the overpotential lowers sharply with decreasing soc in the discharge

**Table 4**  
Physicochemical properties.

Parameters	Symbols	Value	Unit	Ref.
Specific surface area	$A_s$	$1.62 \times 10^4$	m <sup>-1</sup>	[32]
Carbon fiber diameter	$d_f$	$1.76 \times 10^{-5}$	m	[32]
Kozeny-Carman constant	$k_{CK}$	5.55	-	[13]
Local mass transfer coefficient in the pores	$k_m$	$1.6 \times 10^{-4} v^{0.4}$	m s <sup>-1</sup>	[13]
Electronic conductivity of carbon material	$\sigma_s$	1000	S m <sup>-1</sup>	[13]
Proton conductivity of the membrane	$\sigma_m$	$7.3e^{[1268(1/298-1/T)]}$	$\Omega^{-1}m^{-1}$	[28]
Electro-osmotic drag coefficients of water	$n_{d,w}$	2.5	-	[28]
Viscosity of electrolyte	$\mu$	$4.928 \times 10^{-3}$	Pa s	[27]
Densities of electrolyte, water	$\rho$	$1.5 \times 10^3, 1.0 \times 10^3$	kg m <sup>-3</sup>	-
Diffusivity of V <sup>2+</sup>	$D_{V_2}^0$	$2.4 \times 10^{-10}$	m <sup>2</sup> s <sup>-1</sup>	[31]
Diffusivity of V <sup>3+</sup>	$D_{V_3}^0$	$2.4 \times 10^{-10}$	m <sup>2</sup> s <sup>-1</sup>	[31]
Diffusivity of VO <sup>2+</sup>	$D_{V_4}^0$	$3.9 \times 10^{-10}$	m <sup>2</sup> s <sup>-1</sup>	[31]
Diffusivity of VO <sub>2</sub> <sup>+</sup>	$D_{V_5}^0$	$3.9 \times 10^{-10}$	m <sup>2</sup> s <sup>-1</sup>	[31]
Diffusivity of H <sup>+</sup>	$D_{H^+}^0$	$9.312 \times 10^{-9}$	m <sup>2</sup> s <sup>-1</sup>	[27]
Standard reaction rate constants for negative electrode and positive electrode	$k_{neg}, k_{pos}$	$7.0 \times 10^{-8}, 6.8 \times 10^{-7}$	m s <sup>-1</sup>	[27]
Standard equilibrium voltage of VRFB	$E_0$	1.26	V	[27]



(a) charge/discharge voltage



(b) soc evolution curve

**Fig. 3.** Charge/discharge voltage curves and soc evolution curves at various current densities of 20, 40, 60 and 80 mA cm<sup>-2</sup>.

process at the beginning, which is then slowed down until reaching minimum at soc of 0.5. After that, the overpotential increases again with decreasing soc and the variation of overpotential becomes sharper at the end of charge process. Similar behavior is observed for discharge process. This behavior can be explained as follows. At the beginning and the end of charge/discharge process, the concentration of one kind of vanadium ion in certain reactant couples is approaching zero, which thus lowers the reaction kinetics and increases activation polarization. Nevertheless, the depletion of active reactant at the end of charge/discharge process also results in severe concentration polarization. Notice that the variation trend of overpotential with soc is consistent with the simulated results with a pore-scale model [26].

To reveal battery performances, the variations of system charge capacity, system charge/discharge power density, total charge/discharge energy, and system efficiencies with applied current density ranging from 20 to 80 mA cm<sup>-2</sup> are plotted in Fig. 5. Clearly, as can be seen, the system charge capacity is significantly decreased with applied current density, as the result of reduced useful operation window of soc. With the increase of the current density from

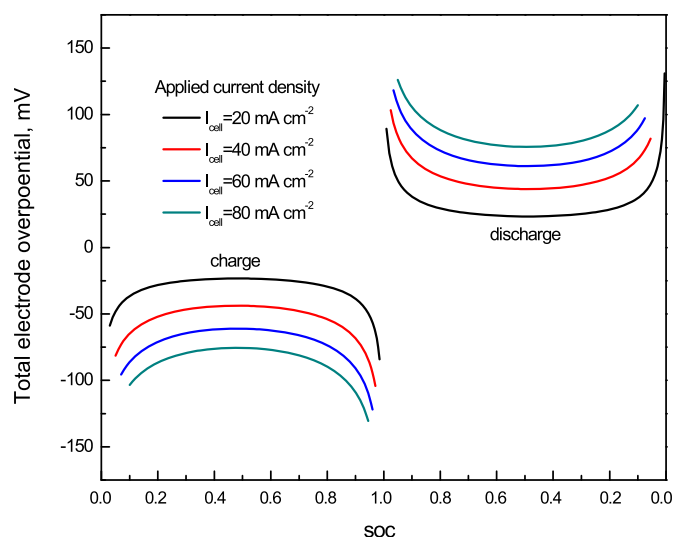


**Fig. 4.** Variations total electrode overpotentials in a charge-discharge cycle at various current densities of 20, 40, 60 and 80 mA cm<sup>-2</sup>.

20 to 80 mA cm<sup>-2</sup>, the system charge capacity is lowered by about 13%. In order to achieve higher system capacity, relatively lower applied current density (i.e., 20–40 mA cm<sup>-2</sup>) is actually preferred from this point of view. However, it is shown that low applied current density leads to low system charge/discharge power density. The mean charge/discharge power densities are almost linearly increased with current density. Therefore, relatively higher current density (i.e., 60–80 mA cm<sup>-2</sup>) may be wanted in order to achieve higher system power and reduce charge/discharge time. With respected to net discharge energy in a charge-discharge cycle, it can be maintained at relatively high level for low applied current densities (i.e., 20–40 mA cm<sup>-2</sup>), which obviously decreases with increasing current density due to the decrease of system capacity. As for the round-trip efficiency, it is lowered from 94% to 83% with varying current density from 20 to 80 mA cm<sup>-2</sup>, because the mean charge voltage is increased and the mean discharge voltage is decreased with the increase of current density resulting from the increased potential losses. Practically, taking into account the pump work consumption, the energy-based system efficiency is obviously reduced in comparison to round-trip efficiency. At the current density of 20 mA cm<sup>-2</sup>, the energy-based efficiency is only about 77% although round-trip efficiency is the maximum. The reason is due to that at low current density of 20 mA cm<sup>-2</sup>, total pump work consumptions in a charge-discharge cycle is very high due to long charge/discharge time, which thus increases total charge energy and decreases net discharge energy in a cycle. With the increase of current density, although the work consumption by pump is decreased, the theoretical efficiency of battery is also decreased losses due to the increased polarizations. A tradeoff between these opposite impacts finally determines the variation trend of energy-based efficiency with current density. As can be seen, energy-based efficiency firstly increases with current density until maximum value of about 80.9% is reached at current densities of 40–50 mA cm<sup>-2</sup>, which is slightly decreased with further increasing current density.

In summary, as revealed in Fig. 5, although low operation current density can achieve high system capacity and high net discharge energy, system power density is low and the charge/discharge time is long. Nevertheless, too low current density also results in low energy-based efficiency. Oppositely, high operation current density is preferred for high system power and short charge/discharge time, but system capacity and net discharge

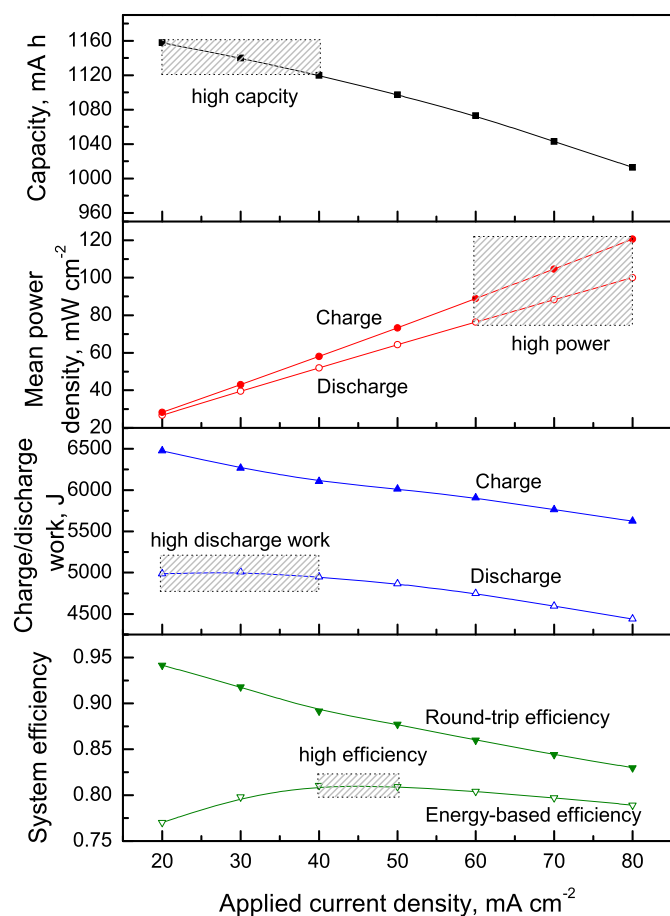


Fig. 5. Effect of various current densities on system capacity, mean power densities, total charge/discharge work in a cycle and system efficiencies.

energy are both low. In order to boost overall charge/discharge performance in view of all performance indicators mentioned-above, the strategies of soc-dependent operating current for charge/discharge process are proposed and explored in the following.

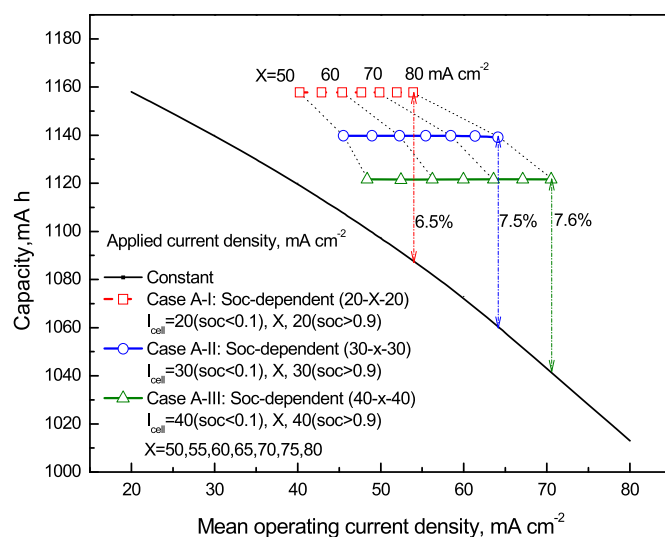
### 3.3. Charge-discharge performance under variable operating current

The influences of various strategies of soc-dependent current density on battery performance are examined in this section. The purpose is to extend useful window of soc such that system capacity can be increased, while high system power and considerable efficiency can be simultaneously maintained.

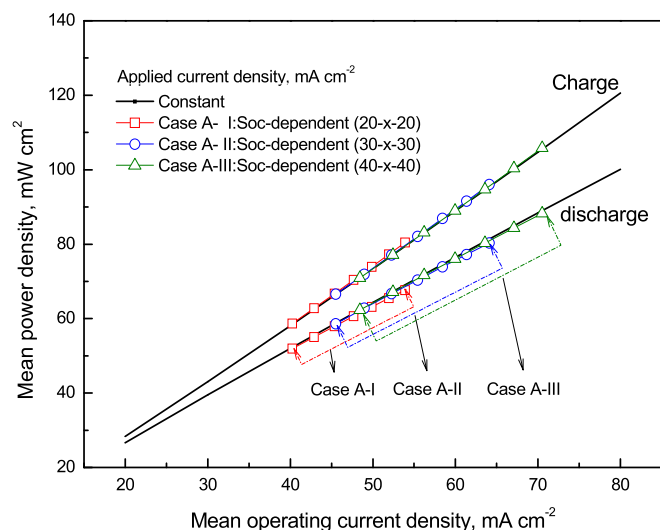
#### 3.3.1. Low current at the beginning and the end (strategy A)

In this strategy, the battery is operated with relatively low current densities (i.e., Case A-I: 20 mA cm<sup>-2</sup>, Case A-II: 30 mA cm<sup>-2</sup>, Case A-III: 40 mA cm<sup>-2</sup>) at the beginning and the end of charge/discharge process (i.e., corresponding to soc < 0.1 and soc > 0.9), and relatively high current densities (i.e., 50, 55, 60, 65, 70, 75 and 80 mA cm<sup>-2</sup>) for the rest time of a charge-discharge cycle.

Fig. 6 shows the impacts of various soc-dependent current densities on system charge capacity and mean charge/discharge power density. To comparatively analyze the result for various soc-dependent current densities and various constant current densities, mean operating current density defined in Eq. (28) is employed. As shown in Fig. 6a, operating the VRFB with soc-dependent current,



(a) charge capacity



(b) Mean charge/discharge power density

Fig. 6. Effect of soc-dependent current density on (a) system charge capacity and (b) mean charge/discharge power density. Case A: relatively low current density (20–40 mA cm<sup>-2</sup>) at the beginning and the end of charge/discharge process, and relatively high current density (50–80 mA cm<sup>-2</sup>) for rest time.

the system capacity for each case (i.e., Case A-I, Case A-II and Case A-III) can be maintained at nearly same value as that under low current operation as the result of extended soc operational window. Using Case A-II as an example, with keeping the current density of 30 mA cm<sup>-2</sup> for the beginning and the end of charge/discharge process while varying the current density for the rest time from 50 to 80 mA cm<sup>-2</sup>, the system charge capacities can be always kept at 1140 mA h for different conditions in Case A-II, which is equal to that for constant current density of 30 mA cm<sup>-2</sup>. However, the mean operating current densities for different conditions in Case A-II are actually in the range from 45 to 64 mA cm<sup>-2</sup>. Under the same mean operating current density, the system capacity for the case of soc-dependent operating current is obviously improved as compared with that for constant-current operation. Among all cases studied, maximally, the system charge capacity can be improved by 7.6% as compared with that operated at mean operating current density of 70 mA cm<sup>-2</sup>. This result implies that with



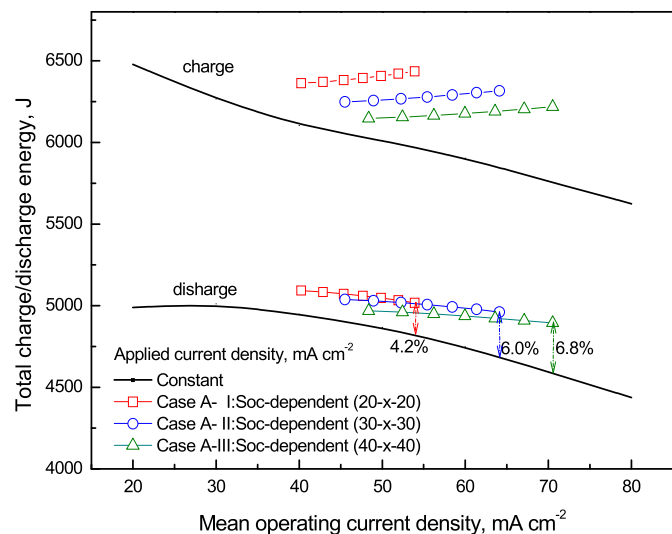


Fig. 7. Effect of soc-dependent current densities (Case A) on total charge energy and discharge energy in a charge-discharge cycle.

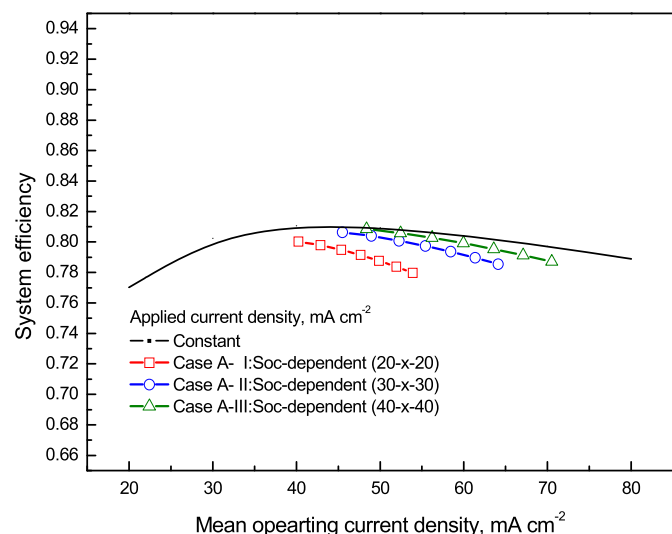


Fig. 8. Effect of soc-dependent current densities (Case A) on energy-based system efficiency.

the strategy of soc-dependent current operation, higher system capacity can be achieved at relatively higher mean operating current density, which is also beneficial for improving system power. As clearly indicated in Fig. 6b, for each case (i.e., corresponding to same system charge capacity), the system mean charge/discharge power densities are dramatically boosted because the mean operating current density is practically shifted to high levels. For instance, if maintaining the system charge capacity at 1140 mA h, the system discharge power density is only 39.3 mW cm<sup>-2</sup> for battery operated at constant current density of 30 mA cm<sup>-2</sup>. However, it ranges from about 58.7 to 80 mW cm<sup>-2</sup> for the battery operated with soc-dependent current densities for Case A-II. Comparing different cases, Case A-III can result in the highest maximum system charge/discharge power density, which is accompanied with tiny sacrifice of system capacity.

Fig. 7 also presents the total charge and discharge energy in a cycle for various soc-dependent current densities. Clearly, operating the battery with soc-dependent current density, the net

discharge energy in a charge-discharge cycle can be increased due to the increased system charge capacity as compared with constant current operation. Using Case A-II as an example, the net discharge energy can be maximally increased by 6% at the mean operating current density of 64 mA cm<sup>-2</sup> as compared with that for constant current operation. Overall, the magnitudes of net discharge energy for all conditions for Strategy A are reaching and even exceeding the maximum net discharge energy of the battery under constant current operation. Correspondingly, the energy-based system efficiencies for various soc-dependent current densities are also illustrated in Fig. 8. Under the precondition of same system capacity, for Case A-I, the energy-based system efficiency is actually increased in comparison with that under constant current density of 20 mA cm<sup>-2</sup>. This is mainly due to the reason that for soc-dependent current, the mean operating current density is actually shifted to high levels, thus significantly lowering the charge/discharge time and reducing pump work consumption. For Case A-II and Case A-III, the energy-based system efficiency can be maintained at comparable level as that for constant current operation. For each case, the system efficiency is slightly decreased with the increase of mean operating current density. Under the precondition of same operating current density (corresponding to same system power density), the energy-based system efficiency for Case A-III is the highest as compared with other two cases, which is actually accompanied with a slight decrease in system capacity. Generally, for all cases involved, the energy-based system efficiencies can be maintained within the range from 78% to 80.9%.

### 3.3.2. Low current at the end (Strategy B)

In this strategy, relatively low current density (i.e., Case B-I: 20 mA cm<sup>-2</sup>, Case B-II: 30 mA cm<sup>-2</sup>, Case B-III: 40 mA cm<sup>-2</sup>) is applied at the end of charge/discharge process (i.e.,  $soc > 0.9$  for charge process and  $soc < 0.1$  for discharge process) while relatively high current density (i.e., 50, 55, 60, 65, 70, 75 and 80 mA cm<sup>-2</sup>) is applied for the rest time. Theoretically, Strategy B may result in higher operating current density with same system capacity as compared with Strategy A.

Fig. 9a presents the comparisons of system capacities under constant applied current densities and soc-dependent current densities for both Strategies A and B. With maintaining the same system capacity, the equivalent operation current density of battery can actually be further extended for strategy B as compared with Strategy A. As can be seen, the maximum equivalent applied current densities for Case B-I, Case B-II and Case B-III can, respectively, be extended to 63.4, 70, and 74 mA cm<sup>-2</sup>, whereas they are, respectively, 54, 64 and 70.4 mA cm<sup>-2</sup> for Case A-I, Case A-II and Case A-III as indicated in Fig. 6. Correspondingly, the mean system discharge power density can be further increased for Strategy B as compared with Strategy A while keeping the same system capacity, as indicated in Fig. 9b. For example, the maximum mean discharge power density is actually increased from 80.4 to 87.2 mW cm<sup>-2</sup> by 9% when comparing Case B-II with Case A-II. Under the precondition of same system power density, the system charge capacity for Case B-I is the highest, which is followed by Case B-II and Case B-III. And, the charge capacity of the battery under soc-dependent current density is much higher than that under constant current operation. Maximally, the system charge capacity is improved by about 8.8%–9.3% for Strategy B as compared with constant-current operation. Fig. 9c also shows the net discharge energy in a charge-discharge cycle under various soc-dependent current densities for Strategy B and Strategy A. As can be seen, at same mean operating current density, the net discharge energy for Case B-I is slightly improved as compared with Case A-I, whereas they are nearly the same for other cases. As compared with that for constant-current operation, the net discharge energy is maximally increased by 6.8%, 7.9% and 7.7%

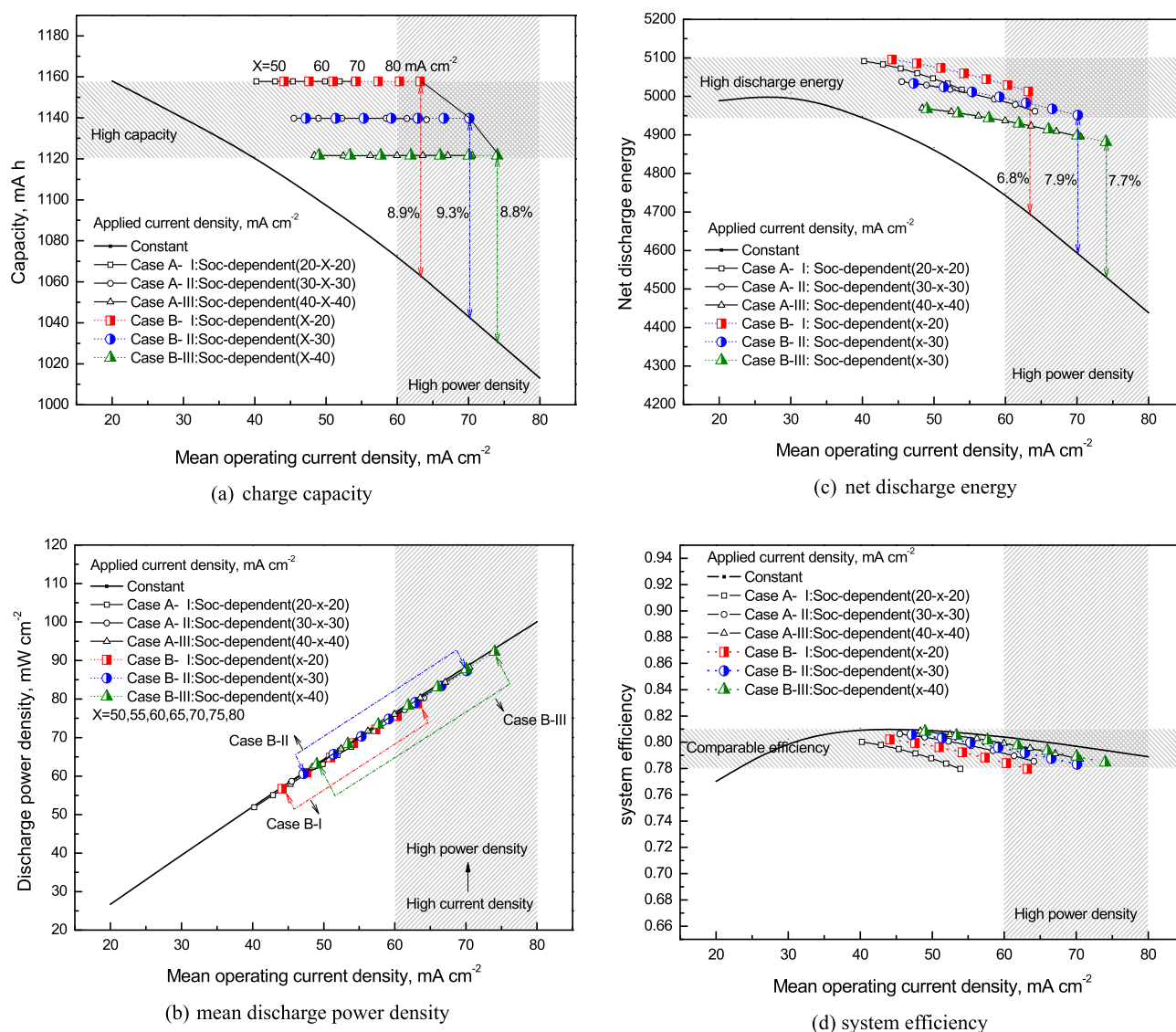


**Fig. 9.** Comparisons of different strategies of soc-dependent current density on (a) mean discharge power density, (b) charge capacity, (d) net discharge energy and (d) system efficiency. Case A: relatively low current density at the beginning and the end of charge/discharge process. Case B: relatively low current density at the end of charge/discharge process.

for Case B-I, Case B-II and Case B-III, respectively. Nevertheless, the values of net discharge energy in a cycle for Case B-I and Case B-II are reaching and even higher than the maximum value of net discharge energy under constant-current operation. Correspondingly, the energy-based system efficiencies under various soc-dependent current densities for both Strategy B and Strategy A are also plotted in Fig. 9d. Under the precondition of same system capacity, the system efficiency for Strategy B is slightly increased as compared with Strategy A, especially for Case B-I. Generally, the system efficiency can be maintained in the range of 78%–80.9% under various conditions of Strategy B. For Case B-II and Case B-III, the system efficiencies are comparable with that for constant-current operation at same operating current density.

In summary, it is suggested that operating the battery with soc-dependent current density for Case B-II, high system capacity, power density, net discharge energy and comparable efficiency can be simultaneously achieved, meaning that overall battery performance is improved.

#### 4. Conclusions

A 2-D quasi-steady-state model is presented to investigate the effects of various constant current densities and various strategies of variable (i.e., soc-dependent) current density on charge/discharge behavior and performance of a VRFB. The main findings are as follows:

- (1) For the battery operated with constant-current, lower applied current density can result in higher system capacity and net discharge energy in a charge-discharge cycle whereas system power density is much lower and the charge/discharge time is much longer. Nevertheless, too low applied current density also leads to low system efficiency because of increased pump work consumption. On the contrary, high current density can achieve high power density but system capacity and net discharge energy in a charge-discharge cycle are low. It is difficult to give consideration

to both system capacity and power density such that overall system performance can be evaluated.

- (2) When the battery is operated with variable (i.e. soc-dependent) current, the system charge capacity, mean power density and net discharge energy in a cycle can be simultaneously boosted while comparable efficiency can be achieved, especially for Strategy B (i.e., low current at the end of charge/discharge process while high current for the rest time). At mean operating current density of about  $70 \text{ mA cm}^{-2}$ , maximally, the system capacity for Case B-II is increased by 9.3% and the net discharge energy for Case B-II is increased by 7.9% in comparison with that for constant-current operation. As for corresponding system efficiency, it can be maintained at about 78.3%, comparable with that for constant-current operation.

## Acknowledgements

This work was supported by the National Key Research and Development Program of China (No. 2017YFB0102703), the National Natural Science Foundation of China (No. 51536003), and Shaanxi Province Youth Science & Technology New Star Plan (2016KJXX-56).

## References

- [1] C. Álvaro, J. Martins, N. Rodrigues, F.P. Brito, *Int. J. Energy Res.* 39 (2015) 889–918.
- [2] K.L. Huang, X.G. Li, S.Q. Liu, N. Tan, L.Q. Chen, *Renew. Energy* 33 (2008) 186–192.
- [3] P. Alotto, M. Guarnieri, F. Moro, *Renew. Sustain. Energy Rev.* 29 (2014) 325–335.
- [4] A.Z. Weber, M.M. Mench, J.P. Meyers, P.N. Ross, J.T. Gostick, Q. Liu, *J. Appl. Electrochem.* 41 (2011) 1137–1164.
- [5] A. Parasuraman, T.M. Lim, C. Menictas, M. Skyllas-Kazacos, *Electrochim. Acta* 101 (2013) 27–40.
- [6] C. Choi, S. Kim, R. Kim, et al., *Renew. Sustain. Energy Rev.* 69 (2017) 263–274.
- [7] M. Christine, K. Ulrich, T. Thomas, *J. Power Sources* 342 (2017) 116–224.
- [8] A.A. Shah, M.J. Watt-smith, F.C. Walsh, *Electrochim. Acta* 53 (2008) 8087–8100.
- [9] X.L. Zhou, T.S. Zhao, L. An, et al., *J. Power Sources* 339 (2017) 1–12.
- [10] K. Oh, H. Yoo, J. Ko, S. Won, H. Ju, *Energy* 81 (2015) 3–14.
- [11] X.K. Ma, H. Zhang, F. Xing, *Electrochim. Acta* 58 (2011) 238–246.
- [12] Y.A. Gandomi, D.S. Aaron, T.A. Zawodzinski, M.M. Mench, *J. Electrochem. Soc.* 163 (2016) A5188–A5201.
- [13] Q. Xu, T.S. Zhao, P.K. Leung, *Appl. Energy* 105 (2013) 47–56.
- [14] J. Houser, A. Pezeshki, J.T. Clement, D. Aaron, M.M. Mench, *J. Power Sources* 351 (2017) 96–105.
- [15] T. Jyothi Latha, S. Jayanti, *J. Power Sources* 248 (2014) 140–146.
- [16] Q. Xu, T.S. Zhao, C. Zhang, *Electrochim. Acta* 142 (2014) 61–67.
- [17] T.J. Latha, S. Jayanti, *J. Appl. Electrochem.* 44 (2014) 995–1006.
- [18] K. Oh, S. Won, H. Ju, *Electrochim. Acta* 181 (2015) 13–23.
- [19] X. You, Q. Ye, P. Cheng, *Int. Commun. Heat. Mass Trans.* 75 (2016) 7–12.
- [20] X.L. Zhou, Y.K. Zeng, X.B. Zhu, L. Wei, T.S. Zhao, *J. Power Sources* 325 (2016) 329–336.
- [21] E. Agar, A. Benjamin, C.R. Dennison, D. Chen, M.A. Hickner, E.C. Kumbur, *J. Power Sources* 246 (2014) 767–774.
- [22] C.Y. Ling, H. Cao, M.L. Cheng, M. Han, E. Birgersson, *J. Power Sources* 294 (2015) 305–311.
- [23] A. Khazaeli, A. Vatani, N. Tahouni, M.H. Panjeshahi, *J. Power Sources* 293 (2015) 599–612.
- [24] X. Ma, H. Zhang, C. Sun, Y. Zou, T. Zhang, *J. Power Sources* 203 (2012) 153–158.
- [25] A. Tang, J. Bao, M. Skyllas-Kazacos, *J. Power Sources* 248 (2014) 154–162.
- [26] G. Qiu, A.S. Joshi, C.R. Dennison, K.W. Knehr, E.C. Kumbur, Y. Sun, *Electrochim. Acta* 64 (2012) 46–64.
- [27] D. You, H. Zhang, J. Chen, *Electrochim. Acta* 54 (2009) 6827–6836.
- [28] W.W. Yang, Y.L. He, Y.S. Li, *Electrochim. Acta* 155 (2015) 279–287.
- [29] C.L. Chen, H.K. Yeoh, M.H. Chakrabarti, *Electrochim. Acta* 120 (2014) 167–179.
- [30] K.W. Knehr, E.C. Kumbur, *Electrochem. Commun.* 13 (2011) 342–345.
- [31] T. Yamamura, M. Watanabe, T. Yano, Y. Shiokawa, *J. Electrochem. Soc.* 152 (2005) A830–A836.
- [32] H.T. Zhou, H.M. Zhang, P. Zhao, et al., *Electrochim. Acta* 51 (2006) 6304–6312.

## Nomenclature

$A_s$ : Specific surface area of porous electrode,  $\text{m}^{-2}$   
 $C$ : Concentration,  $\text{mol m}^{-3}$   
 $d_f$ : Carbon electrode fiber diameter, m  
 $D$ : Diffusivity,  $\text{m}^2 \text{s}^{-1}$   
 $E_0$ : Standard thermodynamic voltage of a VRFB, V  
 $E_{\text{cell}}$ : Voltage of a VRFB, V  
 $E_{\text{eq}}$ : Equilibrium open circuit voltage of a VRFB, V  
 $F$ : Faraday's constant,  $\text{C mol}^{-1}$   
 $\vec{T}$ : Local current density vector,  $\text{A m}^{-2}$   
 $I_{\text{cell}}$ : Operating current density of battery,  $\text{A m}^{-2}$   
 $\bar{I}_{\text{cell}}$ : Average operating current density,  $\text{A m}^{-2}$   
 $j$ : Faradic volumetric current density,  $\text{A m}^{-3}$   
 $k$ : Reaction rate constant,  $\text{m s}^{-1}$   
 $k_m$ : Local mass transfer coefficient,  $\text{m s}^{-1}$   
 $k_{CK}$ : Kozeny-carman constant  
 $K$ : Hydraulic permeability of porous medium,  $\text{m}^2$   
 $L$ : Length of electrode, m  
 $m$ : Source term for mass continuity equation,  $\text{kg m}^{-3} \text{s}^{-1}$   
 $N_w$ : Water crossover flux through the membrane,  $\text{mol m}^{-2} \text{s}^{-1}$   
 $n_{d,w}$ : Electro-osmotic drag coefficients of water  
 $p$ : Liquid pressure, Pa  
 $P_{\text{pump}}$ : Pump power, W  
 $\bar{P}$ : Mean power density,  $\text{W m}^{-2}$   
 $Q$ : Volumetric flow rate of electrolyte,  $\text{ml s}^{-1}$   
 $R$ : Universal gas constant,  $\text{J mol}^{-1} \text{K}^{-1}$   
 $R_i$ : Source term in species conservation equation,  $\text{mol m}^{-3} \text{s}^{-1}$   
 $\text{soc}$ : State of charge  
 $S_\phi$ : Source term in charge conservation equation,  $\text{A m}^{-3}$   
 $t$ : Discharge time, s  
 $T$ : Temperature, K  
 $\vec{u}$ : Superficial liquid velocity vector,  $\text{m s}^{-1}$   
 $v_{in}$ : Superficial velocity at inlet along y direction,  $\text{m s}^{-1}$   
 $V_{\text{tank}}$ : Volume of electrolyte solution,  $\text{m}^3$   
 $z$ : Charge number of the ionic species

## Greek

$\alpha$ : Transfer coefficient  
 $\epsilon$ : Porosity  
 $\eta$ : Overpotential, V  
 $\phi_e$ : Potential in liquid electrolyte phase, V  
 $\phi_s$ : Potential in solid electron-conducting phase, V  
 $\sigma_e$ : Ionic conductivity in liquid electrolyte,  $\text{S m}^{-1}$   
 $\sigma_m$ : Proton conductivity of the membrane,  $\text{S m}^{-1}$   
 $\sigma_s$ : Electronic conductivity of carbon material,  $\text{S m}^{-1}$   
 $\mu$ : Dynamic viscosity, Pa s  
 $\xi$ : Dilution or concentrating factor  
 $\zeta$ : Pump efficiency

## Subscript

*cross*: Cross-section or crossover  
 $e$ : Electrolyte phase  
 $eq$ : Equilibrium  
 $i$ : Species i  
 $in$ : Inlet value  
 $m$ : Membrane  
 $neg$ : Negative  
 $ohm$ : Ohmic  
 $out$ : Outlet value  
 $pos$ : Positive  
 $s$ : Solid phase  
 $w$ : Water

## Superscript

*eff*: Effective value  
 $in$ : Inlet value  
 $s$ : Surface of active reaction site  
 $0$ : Initial value